Magnetic Resonance Imaging 70 (2020) 29–35

Contents lists available at ScienceDirect

Magnetic Resonance Imaging

journal homepage: www.elsevier.com/locate/mri

Original contribution

Intracranial iron distribution and quantification in aceruloplasminemia: A case study

Liche Zhou[a,1], Yan Chen[b,1], Yan Li[c], Sara Gharabaghi[e], Yongsheng Chen[d], Sean K. Sethi[e,f], Yiwen Wu[a,*], E.M. Haacke[a,e,f,**]

[a] Department of Neurology, Institute of Neurology, Ruijin Hospital affiliated with Shanghai Jiao Tong University School of Medicine, Shanghai, China
[b] Department of Neurology, Shandong Provincial Hospital, Jinan, China
[c] Department of Radiology, Ruijin Hospital affiliated with Shanghai Jiao Tong University School of Medicine, Shanghai, China
[d] Department of Neurology, Wayne State University, Detroit, MI, USA
[e] Magnetic Resonance Innovations, Bingham Farms, MI, USA
[f] Department of Radiology, Wayne State University, Detroit, MI, USA

ARTICLE INFO

Keywords:
Aceruloplasminemia
Iron
Brain
R2*-based imaging
Quantitative susceptibility mapping

ABSTRACT

Objectives: Aceruloplasminemia (ACP) is a rare autosomal recessive disorder characterized by intracranial and visceral iron overload. With R2*-based imaging or quantitative susceptibility mapping (QSM), it is feasible to measure iron in the brain quantitatively, although to date this has not yet been done for patients with ACP. The aim of this study was to provide quantitative iron measurements for each affected brain region in an ACP patient with the potential to do so in all future ACP patients. This may shed light on the link between brain iron metabolism and the territories affected by ceruloplasmin function.

Methods: We imaged a patient with ACP using a 3T magnetic resonance imaging scanner with a fifteen-channel head coil. We manually demarcated gray matter and white matter on the Strategically Acquired Gradient Echo (STAGE) images, and calculated values for susceptibility and R2* in these regions. Correlation analysis was performed between the R2* values and the susceptibility values.

Results: Besides the usual territories affected in ACP, we also discovered that the mammillary bodies and the lateral habenulae had significant increases in iron, and the hippocampus was severely affected both in terms of iron content and abnormal tissue signal. We also noted that the iron in the cortical gray matter appeared to be deposited in the inner layers. Moreover, several pathways between the superior colliculus and the pulvinar thalamus, between the caudate and putamen anteriorly and between the caudate and pulvinar thalamus posteriorly were also evident. Finally, R2* correlated strongly with the QSM data ($R^2 = 0.67$, $t = 6.78$, $p < 0.001$).

Conclusion: QSM and R2* have proven to be sensitive and quantitative means by which to measure iron content in the brain. Our findings included several newly noted affected brain regions of iron overload and provided some new aspects of iron metabolism in ACP that may be further applicable to other pathologic conditions. Furthermore, our study may pave the way for assessing efficacy of iron chelation therapy in these patients and for other common iron related neurodegenerative disorders.

1. Introduction

Aceruloplasminemia (ACP), also known as hereditary ceruloplasmin (CP) deficiency, was first described in 1987 by Miyajima et al. [1]. It is a rare autosomal recessive disorder affecting iron metabolism and is caused by mutations in the CP gene on chromosome 3q22-25 [1–4]. CP is a copper containing ferroxidase enzyme with a single polypeptide chain composed of 1046 amino acid residues, which binds to six copper

Abbreviations: ACP, aceruloplasminemia; CP, ceruloplasmin; CNS, central nervous system; MMSE, mini-mental status examination; HAMD-17, Hamilton depression scale 17-item; HAMA-14, Hamilton Anxiety Scale 14-item; STAGE, Strategically Acquired Gradient Echo; SWI, susceptibility weighted imaging; QSM, quantitative susceptibility mapping; iSWIM, iterative susceptibility weighted imaging and mapping

* Corresponding author.
** Correspondence to: E. M. Haacke, Wayne State University, Department of Radiology, Detroit, MI, USA.
E-mail addresses: wyw11380@rjh.com.cn (Y. Wu), nmrimaging@gmail.com (E.M. Haacke).
[1] These authors contributed equally to this work.

https://doi.org/10.1016/j.mri.2020.02.016
Received 30 December 2019; Received in revised form 7 February 2020; Accepted 27 February 2020

ions. It is synthesized and secreted by hepatocytes, astrocytes, choroid plexus epithelium, and Sertoli cells [1,5]. Copper-bound CP exports iron from the reticuloendothelial system, as it is involved in the conversion of iron from its Fe^{2+} ferrous to the Fe^{3+} ferric state in plasma, with consequent delivery of the iron to cells [6]. Iron can enter neurons only when it is bound to transferrin (TF) in the oxidized state and this is hampered in ACP [7]. As a consequence of decreased cellular iron uptake, the extracellular iron pool increases. Moreover, intracellular iron levels also increase via the iron efflux through ferroportin-1 (FPN1) which is dependent on CP [8].

ACP diagnosis is mainly characterized in imaging by iron accumulation in the brain and viscera and then established in a proband with typical clinical findings and identification of biallelic pathogenic variants in CP by molecular genetic testing. The presence of elevated levels of ferritin, low serum copper or increased hepatic iron concentration are often associated with very low levels to absent serum CP [7,9]. Characteristic clinical findings include: evidence of early-onset macular degeneration with undisturbed diabetes mellitus, anemia, visual acuity [10] and neurologic disturbance [11]. Pathologic studies have shown marked accumulation of iron in the liver, pancreas, retina, and central nervous system (CNS), and a marked loss of neurons in the neostriatum, dentate nucleus, and thalamus. A Japanese study found that movement disorders were usually the first neurological sign of ACP [9], however, in another Caucasian cohort, more than half of the patients initially presented with cognitive and/or psychiatric changes or a combination of non-motor and motor features [12]. Overall, ACP phenotypes have been found to be more heterogeneous than previously thought and neurological manifestations can appear two decades after other clinical symptoms [13]. Deficits in CNS include: bradykinesia, postural instability gait, ataxia, tremor, orofacial dyskinesia, chorea, progressive dementia, behavioral changes, apathy and depression [13–16]. With more than one of the above clinical findings and typical results on laboratory testing, ACP should be suspected in individuals with certain characteristic MRI findings. Abnormal low signals in the liver as well as the striatum, thalamus, and dentate nucleus of the brain on T1- and T2-weighted images are consistent with iron deposition and support a diagnosis of ACP [11]. Until recently, spin echo imaging and gradient echo imaging including susceptibility weighted imaging (SWI) [17] have been the mainstay of visualizing increased iron content in the brain via signal loss in these images. A number of case studies of ACP have clearly identified increases in iron content in deep gray matter, thalamus, cortical gray matter, putamen, red nucleus, dentate nucleus, globus pallidus, superior colliculi and cerebral peduncles [18].

Today MRI offers a means to quantify iron content using either R2*-based imaging or quantitative susceptibility mapping (QSM) [19]. In the ACP patient's brain, the nonheme iron concentration has been shown to exceed 20 mg/100 g fresh weight in almost all regions, while such a high level of iron could only be seen in the globus pallidus in a healthy brain [7]. With quantitative MR mapping, it is feasible to longitudinally track iron in the brain, however, it is difficult to assess efficacy of iron chelation therapy without a standardized and quantified description of ACP in MRI findings [20].

In this paper, we not only note the presence of abnormal iron levels throughout the brain in an ACP patient but also provide quantitative iron measurements for each affected region (the deep gray matter, putamen, caudate, mammillary bodies, lateral habenulae, hippocampus and so on). We also present the possible link between brain iron metabolism and the territories affected by ceruloplasmin function. To our knowledge, these findings have not been described previously and it would be helpful to further understand the disease.

2. Materials and methods

The study was approved by the ethics committee at Ruijin Hospital affiliated with the Shanghai Jiao Tong University School of Medicine. Written informed consent was obtained from the participant.

2.1. Patient data

A 53-year old woman was hospitalized due to a one-year history of progressive cognitive decline, slowness of limb movement and a 21-year medical history of diabetes mellitus. Her spouse and colleagues reported that the patient was irritable, anxious, and easily depressed for the last year. The patient became unable to cope with her routine work and daily life because of the decreased memory and slow responses. Moreover, she presented with mild tremor in both hands and seemed to be hesitating while talking and walking. Neurological examination showed general slowness of reaction and movement, slight tremor, and hypermyotonia associated with the upper extremities. The mini-mental status examination (MMSE) was 23 (she has a college education), the Montreal Cognitive Assessment was 17, the Hamilton depression scale 17-item (HAMD-17) was 24, and the Hamilton Anxiety Scale 14-item (HAMA-14) was 26. Laboratory tests revealed anemia (hemoglobin 10.1 g/dl) and hyperglycemia (glucose 210 mg/dl). Notably, the patient had severe copper-iron disturbance with an extremely low level of ceruloplasmin (< 2.00 mg/dl), low serum level of copper (8.54 μg/dl), low level of serum iron (4.7 μmol/l), high level of ferritin (916.7 ng/ml), and a low percentage of transferrin saturation (11%). Exome sequencing detected a mutation on the CP gene: c.606dupA drift mutation; hence, the diagnosis of ACP was confirmed at the genetic level.

2.2. MR imaging

MR scanning was performed on a 3T Ingenia MRI scanner (Philips Healthcare, Best, The Netherlands), using a fifteen-channel head coil. The acquisition parameters followed the Strategically Acquired Gradient Echo (STAGE) imaging protocol [21]: whole brain coverage with a transverse acquisition, TR/TE = 25/7.5 ms, field-of-view (FOV) = 256 mm × 256 mm, matrix = 384 × 192, slice thickness (TH) = 2 mm, bandwidth = 220 Hz/pixel, flip angles (FAs) = 6° and 24°, a third scan was run with TE = 17.5 ms with a 6° FA. Each scan had an acquisition time (T_{acq}) of 1 min, 53 s (total T_{acq} of just under 6 min). Further, a high resolution SWI scan with a resolution of 0.67 mm × 0.67 mm × 1.34 mm was run with TE_1 = 11 ms, TE_2 = 20 ms, TR = 26 ms, FA = 9° and a T_{acq} of 5 min 47 s. An age-matched healthy control was scanned with the same STAGE parameters for visual comparison.

2.3. Reconstructing the susceptibility and R2* maps

Prior to reconstructing the QSM data, the phase image for the TE = 7.5 ms data was pre-processed as follows: it was unwrapped using Laplacian phase unwrapping [19] and then the background field induced by the air/tissue interface was removed using Sophisticated Harmonic Artifact Reduction for Phase (SHARP) [22] (the radius of the kernel and the threshold in SHARP were 6 pixels and 0.05, respectively). Finally, the iterative susceptibility weighted imaging and mapping (iSWIM) method [23,24] was used to reconstruct QSM data from the pre-processed phase image and a k-space threshold of 0.1 was used. In iSWIM [25], the missing parts of k-space were filled in using geometry-constrained high susceptibility components estimated after each iteration. Due to the very high iron content, only the TE = 7.5 ms images were used to reconstruct the QSM data. R2* maps were created using both echoes for each of the FAs, and then averaged [21].

2.4. Method for tracing whole deep gray matter regions

The deep gray matter was manually demarcated on the STAGE maps by one rater using previously published criteria [26,27]. The caudate nucleus, putamen, globus pallidus, substantia nigra, red nucleus, thalamus, medial thalamus, pulvinar thalamus, mammillary body, and the dentate nucleus were traced bilaterally.

2.5. Measuring susceptibility and R2*

Susceptibility and R2* values were calculated from the entire structure of interest. For correlation analysis, we also traced sixty-eight small regions (approximately 10 voxels or 9 mm^3) throughout the parenchyma which included cortical white and gray matter, deep white and gray matter, the dentate nucleus, the corpus callosum, pons, and cerebellum. The region sizes were kept small enough to avoid signal artifacts from high iron or signal dropout on any of the maps to preserve signal homogeneity within the structure. R2* values were then correlated with the susceptibility values as measured from the QSM data.

3. Results

There are three main findings gleaned from the various images in the ACP subject: the first is the enhanced ability to see iron deposition using high resolution gradient echo imaging, the second is the ability to quantify the tissue properties of the affected regions, and the third is the ability to quantify local iron content. The gradient echo sequences make it easy to see iron deposition in this case even for echo times as short as 7.5 ms although contrast improves as the echo time increases to 17.5 ms. We can see increased levels of iron in the lingual gyrus cortical and cerebellar gray matter, as well as in the locus coeruleus and the cuneus region gray matter (Fig. 1a, b). High levels of iron are seen in the dentate nucleus, caudate nucleus, putamen (Figs. 1, 2) (but not the globus pallidus (Fig. 1d, e) which had lower iron content increases), the substantia nigra and red nucleus of the midbrain, in the thalamus (except the medial portion which appears to be spared) and pulvinar thalamus (Fig. 1d, e), in the lateral habenulae (Fig. 1d, e), and in multiple connecting pathways including those between the caudate and putamen (Fig. 2), the superior and inferior colliculi the former of which was connected to the lateral geniculate. We also see abnormally high signal in the body of the hippocampus, at the border of the hippocampus which shows a corrugated dark signal (Fig. 3) in the high resolution FA 9°, TE = 11 ms images. Cortical areas abutting the white matter cranially were affected (more specifically, the inner cortical layers are affected but not the outer layers, although the U-fibers may also have been affected bordering the gray matter/white matter boundaries) (Fig. 4). Some structures such as the locus coeruleus, habenula and fiber pathways that were affected are reported here for the first time in ACP patients.

3.1. Iron content and distribution

The iron content for all measured structures is shown in Table 1, where it can be seen that, for this patient, iron content can be 5 to 10 times higher than that in healthy controls. In healthy subjects, susceptibility increases in the deep gray matter with advancing age [26,28]. In this patient, the iron content was markedly higher than the normal ranges in all measured cortical gray matter and deep gray matter structures with the GP being the only exception. Further, this is the first work in which mammillary body iron is reported in an ACP subject; compared to a recent study, the iron content for healthy controls had a mean susceptibility of 54 ± 20 ppb in the mammillary

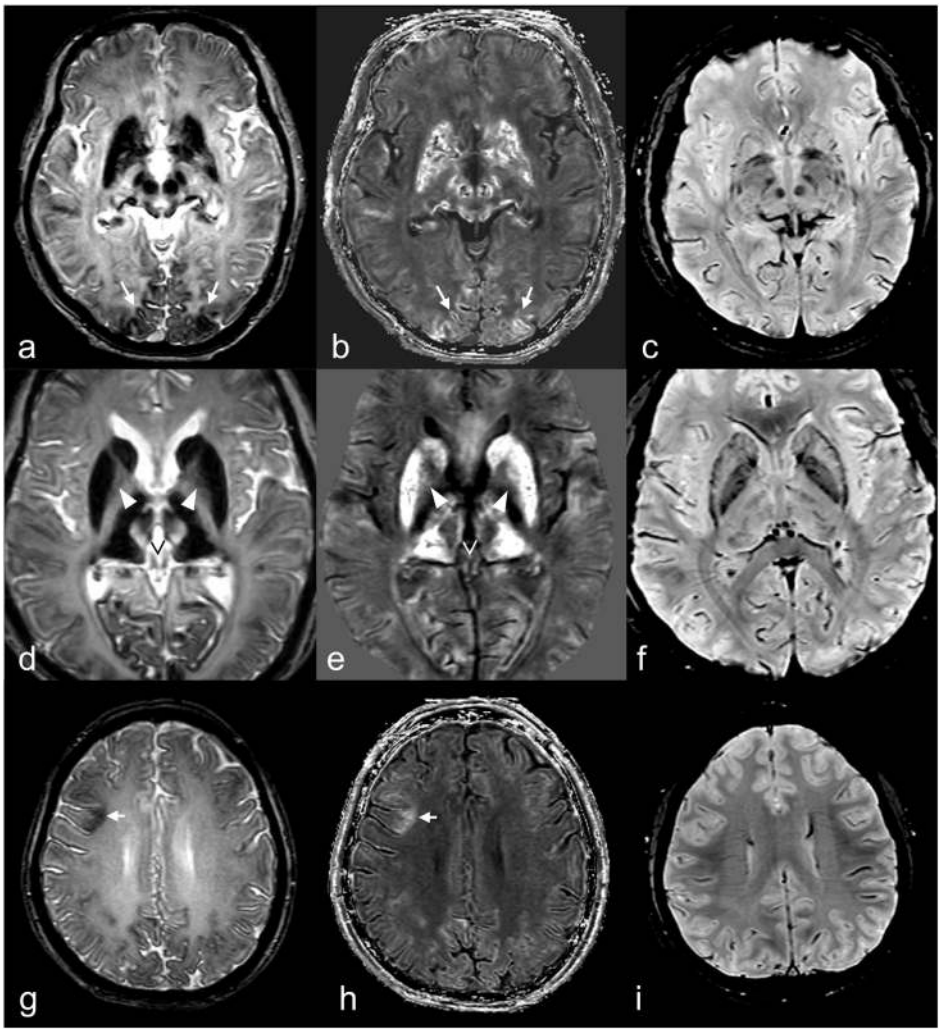

Fig. 1. Images from this ACP subject (left and middle columns) and from an aged-matched healthy control (right column). For the first row: a) magnitude image (TE = 17.5 ms, FA 6°), b) R2* map and c) susceptibility weighted imaging (SWI). White arrows point to iron deposition in the lingual gyrus continuing to the cuneus. For the second row: d) magnitude image (TE = 17.5 ms, FA 6°), e) quantitative susceptibility map (QSM) from the TE = 7.5 ms data and f) SWI. The globus pallidus appears with relatively low iron compared to the putamen within this ACP subject (white triangles in d-e). Connections between the habenula and the pulvinar thalamus along with high iron in the stria medullaris are observed with high iron (top of black V in d, top of white V in e). For the third row: g) magnitude image (TE = 17.5 ms, FA 6°), h) R2* map and i) SWI. Iron deposition is observed in the right precentral gyrus in the magnitude image and the R2* map.

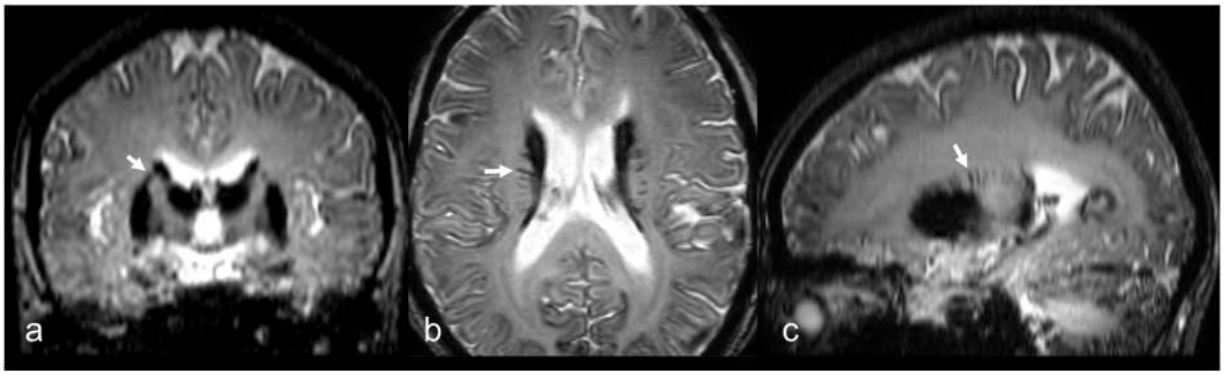

Fig. 2. Long TE (17.5 ms) low flip angle (6°) images showing (a) coronal, (b) transverse and (c) sagittal orientations. White arrows point to connections observed between the caudate nucleus and the putamen.

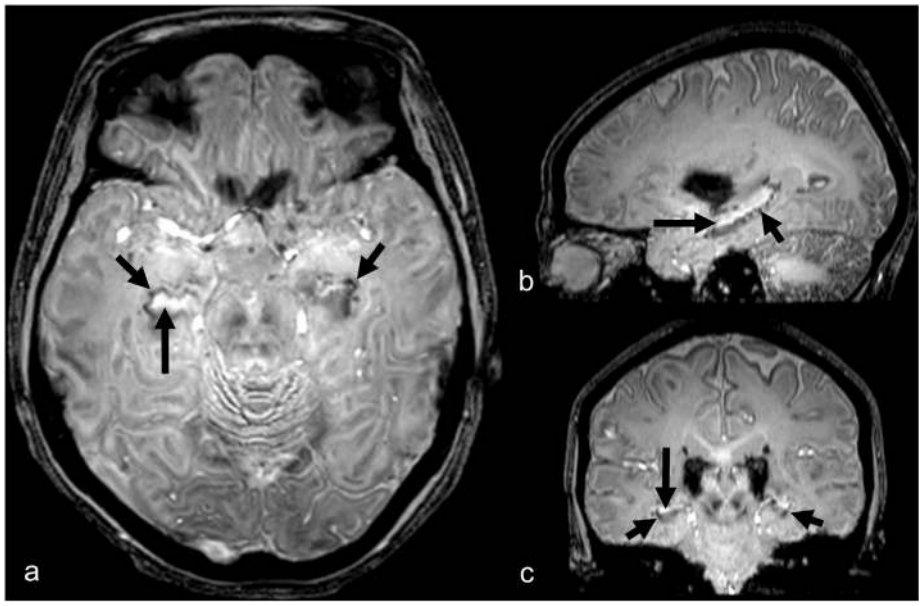

Fig. 3. High resolution images (FA 9°, TE = 11 ms) shown in (a) transverse, (b) sagittal and (c) coronal views. The edge of the hippocampus (short black arrows) shows iron deposition in a corrugated fashion while the interior appears much brighter (long black arrows).

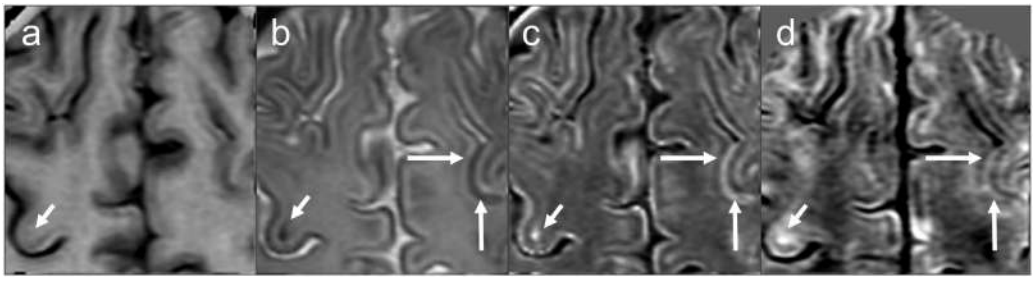

Fig. 4. Cortical areas showing increased iron as seen in a) T1W enhanced (T1WE) images, b) long TE (17.5 ms) low flip angle (6°) image; c) R2* map and d) quantitative susceptibility map. Note that the outer layer of gray matter indicated by the horizontal long arrow has lower iron content than the inner layer denoted by the upward point long arrow. The short arrow in the lower left shows high iron content in what appears to also be gray matter when viewed coronally.

body, roughly four times lower than this ACP patient [29].

For healthy controls, susceptibilities for the substantia nigra, red nucleus, caudate nucleus, putamen, dentate nucleus, and globus pallidus have been reported in the realm of 120 ppb, 90 ppb, 40 ppb, 30 ppb, 110 ppb, and 75 ppb, respectively [28]. Additional susceptibility and R2* values are shown in Table 1 from work by Ghassaban and colleagues [27]. A regional analysis to quantify iron content was performed by Liu and colleagues in which an age-based threshold was applied to the whole structure to preserve only the high-susceptibility pixels. In that work, for healthy controls, the "high-region" iron in the substantia nigra/red nucleus/caudate nucleus/putamen/globus pallidus was measured to be 170–200/120–180/70–105/76–160/208–228 ppb, respectively [26].

R2* vs. QSM yielded a strong correlation (R^2 = 0.67; t = 6.78, $p < 0.001$, Fig. 5). The areas sampled were small, homogeneous regions in the basal ganglia structures, corpus callosum, deep gray matter, cortical gray matter and hippocampus.

Table 1
Susceptibility and R2* values for the basal ganglia, midbrain structures, and dentate nucleus for the ACP subject and 24 healthy controls (from Ghassaban et al. [27]).

	ACP			Healthy controls	
	Volume (mm^3)	Susceptibility (ppb)	R2* (ms)	Susceptibility (ppb)	R2* (ms)
		Mean ± SD	Mean ± SD	Mean ± SD	Mean ± SD
Right Caudate Nucleus	1727	326.0 ± 178.5	137.0 ± 46.8	54.6 ± 6.6	25.2 ± 3.8
Left Caudate Nucleus	1770	438.7 ± 214.5	149.6 ± 53.9	52.4 ± 7.6	24.0 ± 3.9
Right Globus Pallidus	1254	185.6 ± 35.0	92.2 ± 6.0	133.1 ± 10.1	38.4 ± 5.5
Left Globus Pallidus	1332	182.3 ± 65.0	115.0 ± 24.0	127.8 ± 7.8	38.0 ± 5.5
Right Putamen	2978	491.2 ± 281.6	142.6 ± 51.7	68.7 ± 6.4	27.0 ± 3.4
Left Putamen	3132	438.8 ± 261.3	150.1 ± 49.1	72.8 ± 7.0	28.6 ± 3.8
Right Lateral Thalamus	1782	290.2 ± 246.8	141.5 ± 54.7	–	–
Left Lateral Thalamus	2024	323.0 ± 248.6	144.7 ± 49.5	–	–
Right Pulvinar Thalamus	912	560.1 ± 345.9	128.3 ± 56.7	45.3 ± 7.0	21.7 ± 2.2
Left Pulvinar Thalamus	822	689.5 ± 367.8	139.5 ± 57.5	45.6 ± 6.9	21.4 ± 2.1
Right Red Nucleus	322	651.7 ± 307.1	133.6 ± 52.0	108.1 ± 13.0	32.6 ± 4.1
Left Red Nucleus	319	650.6 ± 356.0	128.9 ± 56.6	102.9 ± 12.9	31.9 ± 4.2
Right Substantia Nigra	463	374.6 ± 253.6	115.7 ± 43.5	115.4 ± 11.6	33.7 ± 4.2
Left Substantia Nigra	500	446.6 ± 246.7	129.4 ± 46.0	127.5 ± 10.8	33.4 ± 4.0
Right Dentate Nucleus	1154	822.1 ± 495.2	122.8 ± 59.9	93.1 ± 9.7	29.1 ± 7.9
Left Dentate Nucleus	1130	861.5 ± 526.3	123.7 ± 59.8	95.3 ± 11.0	27.8 ± 6.0
Right Medial Thalamus	807	881.8 ± 204.6	117.5 ± 49.5	–	–
Left Medial Thalamus	820	958.2 ± 150.7	110.9 ± 42.4	–	–
Right Mammillary Body	21	205.9 ± 111.9	61.4 ± 31.4	–	–
Left Mammillary Body	19	240.7 ± 110.2	81.8 ± 49.3	–	

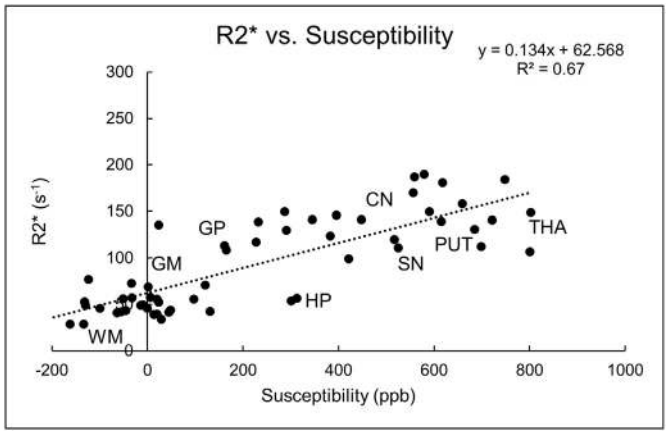

Fig. 5. R2* vs. susceptibility for homogeneous regions of interest throughout the parenchyma yielded a strong correlation ($R^2 = 0.67$, $t = 6.78$, $p < 0.001$). This linear fit gives a susceptibility of roughly −318 ppb for an R2* value of 20/s roughly where the white matter appears. WM, White matter; GM, Gray matter; GP, Globus Pallidus; HP, Hippocampus; CN, Caudate Nucleus; SN, Substantia Nigra; PUT, Putamen; THA, Thalamus.

4. Discussion

Our results show the usual territories affected by ACP such as the basal ganglia, thalamus and cortex as well as several other several key new findings: 1) some fiber pathways could be seen between the superior colliculus and the pulvinar thalamus, between the caudate and putamen anteriorly and between the caudate and pulvinar thalamus posteriorly; 2) the hippocampus was severely affected both in terms of iron content and abnormal tissue signal; 3) the mammillary bodies had significantly high iron; 4) the lateral habenulae had an increase in iron; and 5) the iron manifested mostly in the inner layers of the cortical gray matter with some mild increase apparent in the U-fibers.

From a clinical perspective, we found the deep gray matter and gyri iron accumulation could explain some of the neurological dysfunction. As the caudate, putamen, substantia nigra, red nucleus, and dentate nucleus play important roles in motor control and regulation [30–32], the high iron content in these regions likely explains the extrapyramidal syndromes (bradykinesia, tremor and rigidity) in this patient. The iron accumulation in the prefrontal cortex, thalamus, habenula, and hippocampus (all parts of the prefrontal network and limbic-cortico-striato-pallido-thalamic circuits) which are related to emotion (e.g., depression and anxiety) and cognition [33,34] could explain the patient's emotional problems and cognitive decline. More specifically, the new finding of high iron in the mammillary bodies, which are part of the limbic system and participate in efferenting for recent memory and are involved in episodic or event memory [35–37], may explain the patient's memory impairment and slow response. And for the lateral habenulae, as a key brain region in the pathophysiology of depression [38,39], abnormal iron accumulation there may explain the patient's depression. Some of these clinical and MRI findings have been seen in previous studies [40,41].

ACP has marked iron accumulation in the basal ganglia, midbrain, dentate nucleus and cortex [7]. Based on previous studies, there are several hypotheses for the iron deposition in these specific regions. Firstly, because most of the cellular iron is dispatched to mitochondria and endosomal/lysosomal compartments and participates in oxidative metabolism, intracellular transportation and cellular secretion [42], the high iron content mainly observed in nuclei with highly active metabolism (such as the deep gray matter nuclei) is reasonable. Dysfunction of iron efflux in ACP [8] may aggravate the abnormal iron accumulation in these nuclei. Secondly, iron toxicity likely plays an important role in dopaminergic neurons and interaction with dopamine metabolism [43,44]. Neuromelanin is the end-stage product of dopamine metabolism, which has iron-binding capabilities. When there is an excess of iron that the neuromelanin cannot chelate, the resulting iron overload could cause oxidative stress and lead to neuronal damage. And this leads to a vicious circle that metabolic dysfunction leads to oxidative stress and iron accumulation which then in turn interferes with the metabolism [45]. Thirdly, CP is synthesized and secreted by astrocytes and autopsy studies confirm redox active iron deposited predominantly in the perivascular spaces and terminal astrocytic processes [46,47]. And CP may participate in iron transportation crossing the blood brain barrier (iron recaptured from the ventricular cerebrospinal fluid by the choroidal epithelia and transported into the blood) [42]. This may explain the iron accumulation in the periventricular nuclei and subcortical inner perivascular layers.

In our study, we found iron accumulation in the hippocampus

(Fig. 3) and the inner cortical layers (Fig. 4) over and above that seen in the deep gray matter nuclei. The abnormally high signal within the hippocampus may be due to high iron content which is known to shorten T1 (Fig. 3). Previous studies [48–51] have reported that pyramidal neurons of inner cortical layers and hippocampus were labeled with lactotransferrin and transferrin in both physiological and pathological conditions. Because these pyramidal neurons are metabolically active and rich with iron binding and transport proteins (lactotransferrin and transferrin), iron accumulation in the inner cortical layers and hippocampus makes sense in the condition of CP absence.

We found several pathways between the superior colliculus and the pulvinar thalamus, between the caudate and putamen, anteriorly, and between the caudate and pulvinar thalamus, posteriorly. These were shown as hypointense on the gradient echo magnitude images and hyperintense on the QSM images. As previous studies [52–55] have reported some connectivity and circuits between these nuclei, the pathways may be a consequence of iron deposition in the strands of gray matter that stretch between different nuclei or some terminal astrocytic processes which participant to activate neural signal transmission between these nuclei. However, this hypothesis still needs further pathologic confirmation. Some white matter hyperintensities appear to be present centrally, but this may be caused by the loss of signal from the adjacent gray matter rather than an inherent increase in white matter signal itself.

The map of R2* versus susceptibility revealed a slope of 0.134/s/ppb. This value is similar to that in the recent work of Ghassaban et al. [27] which reports a slope of 0.123/s/ppb. This huge range of iron is not present in the average person where high iron content is perhaps 200 ppb to 300 ppb. In this patient, the iron content was as large as 3 ppm in places, although regions with excessively high iron could not generate a reliable R2* result due to signal loss in the original images and, therefore, they were not plotted. Nevertheless, both R2* and QSM prove to be robust methods for quantifying high iron content in this ACP patient. Potentially either of these measures could be used to track changes in iron content over time during treatment and potentially used to evaluate the therapeutic effect of iron chelation medication [56].

A problem with QSM is that the zero baseline is not absolute. If all the tissues increased their iron content including the white matter and the white matter serves as the zero mark, then for this ACP patient, the white matter will still appear with zero susceptibility. If one assumes that an R2* of 20/s is representative of the usual zero baseline for R2* in healthy controls, then this value of 20/s is reached for the ACP patient when the susceptibility is roughly −318 ppb. That suggests that the true susceptibility should be 318 ppb greater than that quoted in Table 1 for the ACP patient.

4.1. Study limitations/future considerations

One of the problems with a very high level of iron content is avoiding aliasing in the phase data to obtain a good quality QSM image without artifacts. In this study, we used an echo time of 7.5 ms which is already long for some of the highest levels of iron. Ideally this echo time should be closer to 2.5 ms to 5 ms when the susceptibility is on the order of 1 to 3 ppm to produce the best QSM results. Another option would be to scan the patient at 1.5T with 7.5 ms which is equivalent to scanning the patient at 3.75 ms at 3T. Lastly, due to the rarity of the disorder, this study is limited to one subject. The findings presented herein represent the results of this unique case and generalization of any results should be withheld until a larger cohort of subjects can be analyzed.

5. Conclusion

As the mechanisms by which the brain disposes of or stores excess iron are still partly unknown, the findings in this work may help further explore the mechanisms of iron deposition and iron transportation. QSM has proven to be a sensitive and quantitative way to measure iron content in the brain and to map out the distribution of iron. Also, our findings provide some new aspects of iron metabolism in aceruloplasminemia that may be further applicable to other pathologic conditions.

Acknowledgements

We would like to thank the patient for participating in this study.

Funding

This work was supported in part by the National Natural Science Foundation of China Grant number 81870887 and the innovative research team of high-level local universities in Shanghai to Yiwen Wu.

Disclosure

This study was sponsored by the Department of Neurology & Institute of Neurology Ruijin Hospital affiliated with Shanghai Jiao Tong University School of Medicine.

Dr. Liche Zhou reports no disclosures.
Dr. Yan Chen reports no disclosures.
Dr. Yan Li reports no disclosures.
Mrs. Sara Gharabaghi reports no disclosures.
Dr. Yongsheng Chen reports no disclosures.
Mr. Sean K. Sethi reports no disclosures.
Dr. Yiwen Wu reports no disclosures.
Dr. E. M. Haacke reports no disclosures.

References

[1] Miyajima H, Nishimura Y, Mizoguchi K, Sakamoto M, Shimizu T, Honda N. Familial apoceruloplasmin deficiency associated with blepharospasm and retinal degeneration. Neurology 1987;37(5):761–7.
[2] Yoshida K, Furihata K, Takeda S, Nakamura A, Yamamoto K, Morita H, et al. A mutation in the ceruloplasmin gene is associated with systemic hemosiderosis in humans. Nat Genet 1995;9(3):267–72.
[3] Hellman NE, Gitlin JD. Ceruloplasmin metabolism and function. Annu Rev Nutr 2002;22:439–58.
[4] Kono S. Aceruloplasminemia: an update. Int Rev Neurobiol 2013;110:125–51.
[5] Texel SJ, Xu X, Harris ZL. Ceruloplasmin in neurodegenerative diseases. Biochem Soc Trans 2008;36(Pt 6):1277–81.
[6] Gitlin JD. Aceruloplasminemia. Pediatr Res 1998;44(3):271–6.
[7] Miyajima H. Aceruloplasminemia. Neuropathology 2015;35(1):83–90.
[8] Li L, Holscher C, Chen BB, Zhang ZF, Liu YZ. Hepcidin treatment modulates the expression of divalent metal transporter-1, ceruloplasmin, and ferroportin-1 in the rat cerebral cortex and hippocampus. Biol Trace Elem Res 2011;143(3):1581–93.
[9] Miyajima H. Aceruloplasminemia, an iron metabolic disorder. Neuropathology 2003;23(4):345–50.
[10] Yamaguchi M, Nakamura N, Nakano K, Kitagawa Y, Shigeta H, Hasegawa G, et al. Immunochemical quantification of crossline as a fluorescent advanced glycation endproduct in erythrocyte membrane proteins from diabetic patients with or without retinopathy. Diabet Med 1998;15(6):458–62.
[11] Miyajima H, Hosoi Y, Adam MP. Aceruloplasminemia. In: Ardinger HH, Pagon RA, Wallace SE, Bean LJH, Stephens K, editors. GeneReviews((R)). 1993. Seattle (WA).
[12] Vroegindeweij LHP, Langendonk JG, Langeveld M, Hoogendoorn M, Kievit AJA, Di Raimondo D, et al. New insights in the neurological phenotype of aceruloplasminemia in Caucasian patients. Parkinsonism Relat Disord 2017;36:33–40.
[13] Vroegindeweij LH, van der Beek EH, Boon AJ, Hoogendoorn M, Kievit JA, Wilson JH, et al. Aceruloplasminemia presents as Type 1 diabetes in non-obese adults: a detailed case series. Diabet Med 2015;32(8):993–1000.
[14] Kerkhof M, Honkoop P. Never forget aceruloplasminemia in case of highly suggestive Wilson's disease score. Hepatology 2014;59(4):1645–7.
[15] Hellman NE, Kono S, Mancini GM, Hoogeboom AJ, De Jong GJ, Gitlin JD. Mechanisms of copper incorporation into human ceruloplasmin. J Biol Chem 2002;277(48):46632–8.
[16] Di Raimondo D, Pinto A, Tuttolomondo A, Fernandez P, Camaschella C, Licata G. Aceruloplasminemia: a case report. Intern Emerg Med 2008;3(4):395–9.
[17] Liu S, Buch S, Chen Y, Choi HS, Dai Y, Habib C, et al. Susceptibility-weighted imaging: current status and future directions. NMR Biomed 2017;30(4).
[18] Calder GL, Lee MH, Sachithanandan N, Bell S, Zeimer H, MacIsaac RJ. Aceruloplasminaemia: a disorder of diabetes and neurodegeneration. Intern Med J 2017;47(1):115–8.
[19] Haacke EM, Liu S, Buch S, Zheng W, Wu D, Ye Y. Quantitative susceptibility mapping: current status and future directions. Magn Reson Imaging

2015;33(1):1–25.
[20] Marchi G, Busti F, Lira Zidanes A, Castagna A, Girelli D. Aceruloplasminemia: a severe neurodegenerative disorder deserving an early diagnosis. Front Neurosci 2019;13:325.
[21] Chen Y, Liu S, Wang Y, Kang Y, Haacke EM. STrategically Acquired Gradient Echo (STAGE) imaging, part I: creating enhanced T1 contrast and standardized susceptibility weighted imaging and quantitative susceptibility mapping. Magn Reson Imaging 2018;46:130–9.
[22] Schweser F, Deistung A, Lehr BW, Reichenbach JR. Quantitative imaging of intrinsic magnetic tissue properties using MRI signal phase: an approach to in vivo brain iron metabolism? Neuroimage 2011;54(4):2789–807.
[23] Haacke EM, Tang J, Neelavalli J, Cheng YC. Susceptibility mapping as a means to visualize veins and quantify oxygen saturation. J Magn Reson Imaging 2010;32(3):663–76.
[24] Tang J, Liu S, Neelavalli J, Cheng YC, Buch S, Haacke EM. Improving susceptibility mapping using a threshold-based K-space/image domain iterative reconstruction approach. Magn Reson Med 2013;69(5):1396–407.
[25] Wharton S, Schafer A, Bowtell R. Susceptibility mapping in the human brain using threshold-based k-space division. Magn Reson Med 2010;63(5):1292–304.
[26] Liu M, Liu S, Ghassaban K, Zheng W, Dicicco D, Miao Y, et al. Assessing global and regional iron content in deep gray matter as a function of age using susceptibility mapping. J Magn Reson Imaging 2016;44(1):59–71.
[27] Ghassaban K, He N, Sethi SK, Huang P, Chen S, Yan F, et al. Regional high iron in the substantia nigra differentiates Parkinson's disease patients from healthy controls. Front Aging Neurosci 2019;11:106.
[28] Acosta-Cabronero J, Betts MJ, Cardenas-Blanco A, Yang S, Nestor PJ. In vivo MRI mapping of brain iron deposition across the adult lifespan. J Neurosci 2016;36(2):364–74.
[29] Lin Z, Sethi SK, Li B, He N, Chen W, Haacke EM, et al. Susceptibility and volume changes of the mammillary bodies as a function of age for healthy individuals and early stage dementia. Proc. of the ISMRM 27th annual meeting & exhibition in Montréal, Québec, Canada. 2019. Montreal, Quebec, Canada.
[30] Graybiel AM, Aosaki T, Flaherty AW, Kimura M. The basal ganglia and adaptive motor control. Science (New York, NY) 1994;265(5180):1826–31.
[31] Yin HH. The basal ganglia in action. Neuroscientist 2017;23(3):299–313.
[32] Bostan AC, Strick PL. The basal ganglia and the cerebellum: nodes in an integrated network. Nat Rev Neurosci 2018;19(6):338–50.
[33] Price JL, Drevets WC. Neural circuits underlying the pathophysiology of mood disorders. Trends Cogn Sci 2012;16(1):61–71.
[34] Baxter MG, Chiba AA. Cognitive functions of the basal forebrain. Curr Opin Neurobiol 1999;9(2):178–83.
[35] Nelson AJD, Vann SD. The importance of mammillary body efferents for recency memory: towards a better understanding of diencephalic amnesia. Brain Struct Funct 2017;222(5):2143–56.
[36] Rolls ET. Limbic systems for emotion and for memory, but no single limbic system. Cortex 2015;62:119–57.
[37] Vann SD, Aggleton JP. The mammillary bodies: two memory systems in one? Nat Rev Neurosci 2004;5(1):35–44.
[38] Li K, Zhou T, Liao L, Yang Z, Wong C, Henn F, et al. betaCaMKII in lateral habenula mediates core symptoms of depression. Science (New York, NY) 2013;341(6149):1016–20.
[39] Hikosaka O, Sesack SR, Lecourtier L, Shepard PD. Habenula: crossroad between the basal ganglia and the limbic system. J Neurosci 2008;28(46):11825–9.
[40] Pan PL, Tang HH, Chen Q, Song W, Shang HF. Desferrioxamine treatment of aceruloplasminemia: long-term follow-up. Mov Disord 2011;26(11):2142–4.
[41] Bove F, Fasano A. Iron chelation therapy to prevent the manifestations of aceruloplasminemia. Neurology 2015;85(12):1085–6.
[42] Dusek P, Jankovic J, Le W. Iron dysregulation in movement disorders. Neurobiol Dis 2012;46(1):1–18.
[43] Matak P, Matak A, Moustafa S, Aryal DK, Benner EJ, Wetsel W, et al. Disrupted iron homeostasis causes dopaminergic neurodegeneration in mice. Proc Natl Acad Sci U S A 2016;113(13):3428–35.
[44] Jiang H, Song N, Wang J, Ren LY, Xie JX. Peripheral iron dextran induced degeneration of dopaminergic neurons in rat substantia nigra. Neurochem Int 2007;51(1):32–6.
[45] Daugherty AM, Raz N. Appraising the role of iron in brain aging and cognition: promises and limitations of MRI methods. Neuropsychol Rev 2015;25(3):272–87.
[46] Gonzalez-Cuyar LF, Perry G, Miyajima H, Atwood CS, Riveros-Angel M, Lyons PF, et al. Redox active iron accumulation in aceruloplasminemia. Neuropathology 2008;28(5):466–71.
[47] Kaneko K, Hineno A, Yoshida K, Ohara S, Morita H, Ikeda S. Extensive brain pathology in a patient with aceruloplasminemia with a prolonged duration of illness. Hum Pathol 2012;43(3):451–6.
[48] Liu HM, Atack JR, Rapoport SI. Immunohistochemical localization of intracellular plasma proteins in the human central nervous system. Acta Neuropathol 1989;78(1):16–21.
[49] Morris CM, Candy JM, Kerwin JM, Edwardson JA. Transferrin receptors in the normal human hippocampus and in Alzheimer's disease. Neuropathol Appl Neurobiol 1994;20(5):473–7.
[50] Connor JR, Fine RE. The distribution of transferrin immunoreactivity in the rat central nervous system. Brain Res 1986;368(2):319–28.
[51] Leveugle B, Spik G, Perl DP, Bouras C, Fillit HM, Hof PR. The iron-binding protein lactotransferrin is present in pathologic lesions in a variety of neurodegenerative disorders: a comparative immunohistochemical analysis. Brain Res 1994;650(1):20–31.
[52] Berman RA, Wurtz RH. Functional identification of a pulvinar path from superior colliculus to cortical area MT. J Neurosci 2010;30(18):6342–54.
[53] Coude D, Parent A, Parent M. Single-axon tracing of the corticosubthalamic hyperdirect pathway in primates. 223(9). 2018. p. 3959–73.
[54] Shipp S. The functional logic of corticostriatal connections. Brain Struct Funct 2017;222(2):669–706.
[55] Soria G, Wiedermann D, Justicia C, Ramos-Cabrer P, Hoehn M. Reproducible imaging of rat corticothalamic pathway by longitudinal manganese-enhanced MRI (L-MEMRI). NeuroImage 2008;41(3):668–74.
[56] Wang Y, Spincemaille P, Liu Z, Dimov A, Deh K, Li J, et al. Clinical quantitative susceptibility mapping (QSM): biometal imaging and its emerging roles in patient care. J Magn Reson Imaging 2017;46(4):951–71.